ELSEVIER

Nuclear Instruments and Methods in Physics Research B 164–165 (2000) 353–364

NIM B
Beam Interactions with Materials & Atoms

www.elsevier.nl/locate/nimb

Auger electrons from ion tracks

G. Schiwietz [a,*], G. Xiao [a], E. Luderer [a], P.L. Grande [b]

[a] *Hahn-Meitner-Institut, Strukturforschung, Glienicker Str. 100, 14109 Berlin, Germany*
[b] *Instituto de Fisica, Universidade Federal do Rio Grande do Sul, 91500 Porto Alegre, Brazil*

Abstract

The target KVV Auger electron emission has been investigated experimentally and theoretically for heavy-ion irradiation of amorphous carbon at an ion velocity of 14.1 a.u. (5 MeV/u). We extend previous investigations of multiple ionization and electronic nuclear-track temperatures to a large variety of charged projectiles, covering electrons to uranium ions. Experimental data are compared with non-pertubative calculations of multiple ionization and with results of two thermal-spike models.

1. Introduction

Track effects in polymers are known since some decades [1] and have found widespread applications [2] in dosimetry, archeometry, environmental research and in the production of micro-pore filters as well as in the search for mineral resources such as oil and uranium. Some other materials such as alkali halides are so sensitive to electronic excitations that even light projectiles lead to atomic displacements or electronic desorption [3,4]. For these materials, the dominant rearrangement processes seem to occur far away from the ion path and only some specific material-modification effects are influenced by the extraordinary high excitation density in the center of the nuclear track [5]. Track effects due to fast heavy ions in metals, especially in metallic glasses, have been discovered about a decade ago [6] and different explanations for the basic track-production mechanisms have been proposed. The corresponding scenarios are *Coulomb explosion* due to the mutual repulsion of ionized target atoms [1], spontaneous lattice relaxation due to *long lived repulsive states* [7,8] and the thermal spike due to *electron–phonon coupling* [9] or individual *ion–electron collisions* [10].

All these mechanisms may finally yield an unordered atomic motion and if a critical local lattice temperature is exceeded then a permanent atomic rearrangement may result on a time scale of 0.1–10 ps. There are many investigations on changes of macroscopic material parameters, but most of them are related to the asymptotic long-time behavior of the samples. Thus, it is hardly possible to distinguish between the basic mechanisms without

* Corresponding author. Tel.: +49-30-8062-2448; fax: +49-30-8062-2293.
E-mail address: schiwietz@hmi.de (G. Schiwietz).

0168-583X/00/$ - see front matter
PII: S0168-583X(99)01064-2

a sound knowledge on the short-time evolution of the nuclear track.

In previous investigations of Auger electrons and convoy electrons ejected from polymers (polypropylene and mylar) during heavy-ion irradiation we have found evidence for nuclear-track guided (convoy) electrons [11,12] as well as decelerated Auger electrons [13–15]. Both effects are due to the nuclear-track potential resulting from ionization and charge separation in the ion track. The corresponding positive potential attracts electrons and repels positively charged light target ions [16]. For heavy ions with charge states $q > 10$ at 5 MeV/u, the nuclear-track potential is strong enough (>50 eV) and lives long enough (between 2×10^{-14} and 10^{-11} s) to lead at least to a partial Coulomb explosion involving the hydrogen atoms of the polymer. For high projectile charge states with $q \gg 15$, also carbon atoms should acquire high kinetic energies and significant erosion yields have been found for these ions [11,12].

On the contrary, for amorphous carbon (a conductor with low conductivity) no indications for a nuclear-track potential could be found. Neither the Auger measurements [13–15] nor the convoy measurements for amorphous carbon targets [11,12] show similar effects as where found for polymer targets. Thus, the electronic charge neutralization is fast in this material and Coulomb explosion can be excluded.

In this work, we focus our attention on electronic target excitations *during* and *after* the passage of the ion by extending previous investigations [17,18]. We report on Auger electron spectra for single and double K-shell ionization of amorphous carbon. From the intensity ratios it is possible to derive the initial degree of ionization in the center of the track. Furthermore, the slopes of the Auger spectra show the influence of conduction-band excitations. Two electron temperatures for the corresponding Auger-decay times of 6 and 11 fs are extracted from the data and compared with predictions of two thermal-spike models. Furthermore, one of these models is significantly improved in this work. Thus, the present investigation yields information on electronic target excitations in the center of the track for times between 0 and 11 fs after the ion passage.

2. Auger electron analysis

The experiments were performed with fast highly charged particles at a velocity of 10% the speed of light (at 5 MeV/u) delivered by the heavy-ion cyclotron of the Ionenstrahl-Labor (ISL) at the Hahn-Meitner-Institut, Berlin. The beam of 0.1–10 particle nA was focused at the center of a magnetically shielded target chamber (for details see [14,15]). Using a post-cyclotron stripper foil we have selected an initial projectile charge state q close to its solid-state equilibrium value. Thus, the results are nearly independent of the degree of excitation of the projectile.

Thin evaporated amorphous carbon foils (a-C between 3 and 100 $\mu g/cm^2$) with an average hydrogen content of 5–10% have been used. A maximum temperature rise of <100 K is expected inside the substrate for the highest ion flux during the irradiation. Auger electron spectra were taken at an angle of 135° with respect to the incident beam and to the surface normal of the samples using an electrostatic parallel-plate spectrometer that was operated at an energy resolution of 7.5%. As has been shown in a previous work, Auger electrons ejected in backward directions (135°) are induced directly by the projectile (in the central track region). A remaining small fraction of 5–10% is related to δ-electron cascades [19].

We have performed electron irradiations at primary energies between 1.5 and 3 keV. The corresponding Auger spectra show no dependence on the primary energy but on the projectile flux. With increasing particle flux we observed an increasing carbon K-Auger energy (without any change in the peak structure) consistent with the measured reduction of the oxygen KVV-Auger intensity. Thus, there is dynamic cleaning of the surface by electronic desorption. The estimated oxygen coverage after extended irradiation is below 10% for the ion experiments and nearly invisible in the electron spectra taken with 10 μA e^-.

Fig. 1 displays normalized Auger spectra for different projectiles at an energy of 5 MeV/u after subtraction of a continuous background and separation in single- and double-ionization contributions (for details of the data handling procedures see [17,18]). It is emphasized that these spectra

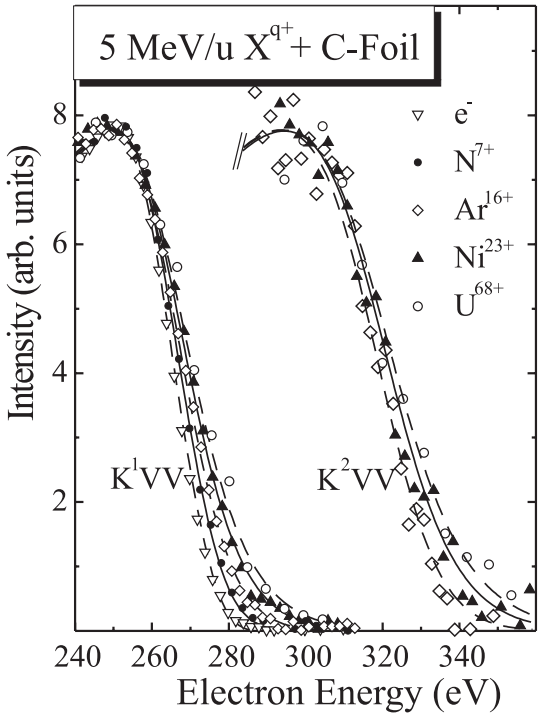

Fig. 1. Normalized Auger electron spectra after background subtraction induced by different charged projectiles of equal speed for single and double K vacancies, K^1VV and K^2VV, respectively.

close to the Auger peak maximum are insensitive to details of the subtracted background. To compensate the influence of different O coverages and an inaccurate energy calibration of previous Ni^{23+} [14,15] and U^{68+} [20] experiments, the electron-energy scales are readjusted at the peak maximum.

Spectra with an accurate energy calibration have been taken for incident electrons as well as for N^{7+} and Ar^{16+} ions in this work and previously also for electrons, O and Kr projectiles taken with higher resolution [17,18]. These spectra indicate that the energy at the peak maximum does not depend on the projectile within ± 0.5 eV. Thus, there is no all-over shift of the spectra and correspondingly there is no track potential when the K vacancy decays. Such a nuclear-track potential decelerates the ejected Auger electrons. For polypropylene targets it was shown to exceed 50 V in the case of heavy ions, since there is no complete charge neutralization during the decay time. From the uncertainty of the determination of the peak position, from theoretical values of the nuclear-track potential [14,15] and under the assumption of an exponential decay of the potential one can conclude that the upper limit of the charge-neutralization time is $\tau_{CN} < 1.5$ fs.

This boundary, extracted from the Auger spectra, is consistent with $\tau_{CN} < 0.3$ fs, as follows from an investigation of convoy electrons ejected in the projectile direction [11,12]. A fraction of these electrons may move behind the projectile and may be decelerated and focussed towards the projectile direction, if there is a significant positive potential 50–100 Å behind the moving projectile. Such nuclear-track guided electrons were not observed for ions with nuclear charges below $Z_P = 30$ in amorphous carbon targets [11,12].

Theoretically, we expect a small perturbation of the valence-band electrons for light projectiles and the charge-neutralization time should roughly be given by the plasmon frequency. On the contrary, for heavy projectiles there is a significant depopulation of the valence band and the electrons have to return from distances of a few Å. From the mean impact parameters of ionization events and from the Fermi velocity as well as additionally from the plasmon frequency one may estimate that the charge-neutralization time τ_{CN} should roughly be 0.1 fs for light ions (for $q \ll 10$) and 0.2 fs for highly charged heavy projectiles, consistent with the experimental results.

All of the estimated times are so short that even the lightest atoms will not gain enough energy to be displaced by the repulsive potential and, hence, Coulomb explosion can clearly be excluded for this material with fast recombination. Further information on the energy deposition and dissipation close to the ion track may be obtained from the investigation of the intensities and shapes of the Auger peaks as will be discussed below.

Fig. 2 displays the ratio of double to single K-shell ionization events in the target as obtained from the Auger spectra. We have used two methods of evaluation and both yield nearly identical results. One may either integrate the Auger spectra from half the peak energy to the high energy edge and divide the result by the escape depths (roughly proportional to $E^{1.7}$, where E is the kinetic electron

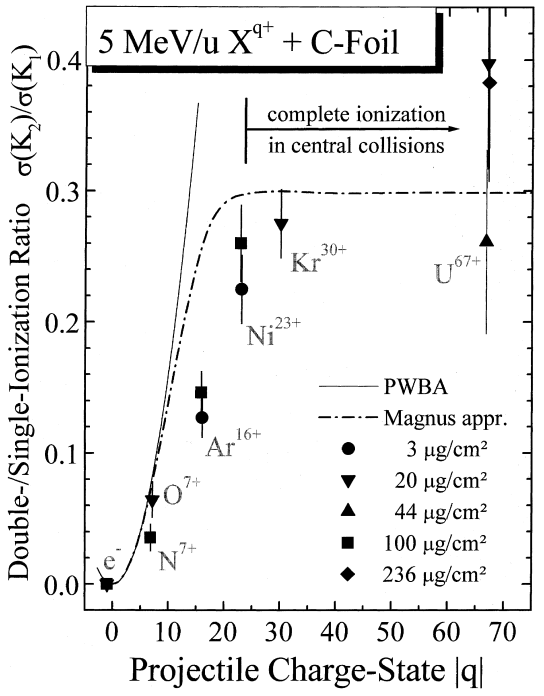

Fig. 2. Ratio of double to single-ionization cross-sections as derived from the K^1VV and K^2VV Auger intensities in comparison with two theoretical estimates.

energy at the peak maximum) or divide the maximum Auger intensity by the mean free inelastic path (roughly proportional to $E/\ln E$) to derive normalized intensities that are nearly independent of the transport properties of Auger electrons. Furthermore, one has to correct for Auger cascades (a singly ionized K-shell follows each K^2VV decay) and δ-electron cascades (dependent on the foil thickness fast δ-electrons produce between 5% and 10% single K vacancies at the ion-entrance side of the foil) that increase the K^1VV peak intensity [14,15,19].

As can be seen from the figure, for incident electrons we have not observed any double-K-shell ionization. For incident ions, however, the double-K-shell contribution increases steadily with the projectile charge state q and reaches a plateau for $q > 25$. This plateau may be interpreted with the help of theoretical results for the cross-section ratio $\sigma(K_2)/\sigma(K_1)$. The thin solid curve denoted PWBA is calculated within first-order perturbation theory for bare ions of charge state q [21]. It is strictly proportional to q^2 and its steepness depends only on the target potential and on the projectile velocity. The dashed–dotted curve is calculated within the Magnus approximation which goes beyond the PWBA treatment. The Magnus approximation accounts for probability conservation by including all direct couplings between the ground state and the continuum states [21]. In this way it includes the so-called saturation effect where ionization probabilities are always restricted to a maximum of 100%, unlike in standard treatments based on perturbation theory. The Magnus results show a similar plateau as the experimental data do and this plateau is an indication for K-shell ionization probabilities close to 100% near the ion path [13]. The same model predicts ionization probabilities of 100% for the weakly bound valence-band electrons already at much larger impact parameters, in agreement with atomic collision knowledge. Hence, the good agreement between experimental data and Magnus results in Fig. 2 shows that the carbon atoms in the center of the track are completely ionized by projectiles with charge states $q > 25$ (at the time $t = 0$).

The striking feature in Fig. 1 is the broadening of the Auger line-structures. The broadening increases with increasing projectile charge and reaches about 5 eV for U^{68+} ions. First, this observation will be discussed from an experimental point of view, before a theoretical treatment is presented in the next section. Since long-lived collective potentials have already been excluded, there are three effects left that could lead to a broadening of Auger structures. The most obvious one is a change of the atomic and electronic target structure during heavy-ion irradiation. In fact, auxiliary measurements of the electrical conductivity point to a change of the amorphous carbon structure. The specific resistance was dropping from roughly 1.6 to 0.06 Ω cm which, however, is still about two orders of magnitude above the values for microcrystalline carbon. This change, however, was not significantly influencing the gross electronic band structure, since electron induced Auger spectra taken before and after the ion irradiation did not show any variation for the

samples. Another effect, namely the nuclear energy transfer due to the close encounter of the projectile with a target atom during K-shell ionization, leads to a kinematic Doppler broadening. This effect, however, is more than an order of magnitude too small in the present cases to be detected in the Auger lines. Thus, the measured broadening must be related to residual electronic excitations in the valence band that will be discussed in the following.

The KVV Auger spectrum results from an empty K-shell state (K) that is filled by one out of two valence-band electrons (VV) that interact with another. Thus, the line shape tests the energy distribution of valence-band electrons during the decay and close to the inner-shell excited atom. Hence, it provides information on the degree of valence-band excitation at about 6 fs (K^2VV) and 11 fs (K^1VV) after the passage of the ion within a cylinder radius of about 1 Å around the ion path. The initial projectile induced excitation is so fast and the Auger decay so slow that a local thermodynamical equilibrium of the electronic subsystem may be assumed [22,23]. Consequently, we will describe the electronic excitations in terms of an electron temperature.

Before we discuss the details of an accurate evaluation of the electron temperature T_e, we present a simple estimate for this quantity. Since the KVV-Auger decay results from the interaction of two valence-band electrons, the high-energy slope of the line is predominantly given by the convolution of the energy distribution (density-of-states, DOS) of two such electrons near the Fermi level. Electrons excited above the Fermi level give then rise to a peak broadening. For a rough estimate of T_e, we assume that the corresponding temperature broadening of the DOS can be described by a convolution with Gaussian shapes. The half width at half maximum of the Auger line is then given by $\Delta E(T_e) = \sqrt{\Delta E_0^2 + 2k^2T_e^2}$. Here, the convoluted DOS (for 0 K), including transport effects and experimental resolution, is represented by an energy width ΔE_0. The temperature broadening is approximately given by kT_e for each of the two electrons, where k is the Boltzmann constant. From $\Delta E_0 = 13.7$ eV and $\Delta E(T_e) = 18.7$ eV, obtained from Gaussian fits to the K^1VV spectra for electrons and uranium ions in Fig. 1, we estimate an electron temperature of $T_e = 10^5$ K for the spectrum induced by uranium ions (assuming $T_e \cong 0$ K for incident electrons).

For a more detailed analysis, however, one should consider the actual DOS of the target. The DOS for the σ and π states of evaporated amorphous carbon (a-C) is shown in the upper part of Fig. 3 as obtained from band-structure calculations in [24,25]. It is seen that there is a pronounced minimum at the Fermi level, but with a finite electron density (unlike in graphite or diamond). At finite temperatures, the energy distribution $n_X(\varepsilon, T_e, T_{\text{lattice}})$ in a given band X of carbon depends then on the partial DOS $D_X(\varepsilon, T_{\text{lattice}})$ according to

$$n_X(\varepsilon, T_e, T_{\text{lattice}}) = D_X(\varepsilon, T_{\text{lattice}}) f(\varepsilon, T_e), \tag{1a}$$

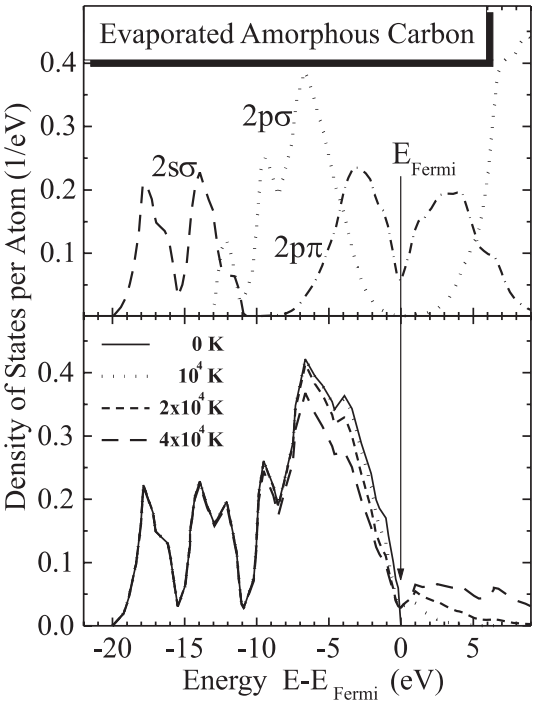

Fig. 3. Partial DOS and total electron-energy distribution for electron temperatures between 0 and 4×10^4 K in evaporated amorphous carbon.

with the Fermi–Dirac distribution

$$f(\varepsilon, T_e) = \frac{1}{1 + \exp[(\varepsilon - \mu)/(k_B T_e)]}, \tag{1b}$$

where the chemical potential μ is chosen to yield the correct volume electron-density N ($N = 4$ electrons per atom)

$$N = \int_0^\infty d\varepsilon \sum_X n_X(\varepsilon, T_e, T_{lattice}). \tag{1c}$$

The high-energy edge of the Auger line-profile depends mainly on convolutions of the energy distributions $D_X(\varepsilon, T_{lattice}) \cdot f(\varepsilon, T_e)$ for all bands, weighted by Auger matrix-elements [26]. As can be seen from the lower part of Fig. 3, an increased temperature leads to a broadening of the electron-energy distribution that should show up in the Auger spectra. Comparison of these distributions with the spectra in Fig. 1 indicates that the corresponding electron temperatures T_e will exceed 40,000 K for the heaviest ions.

For an accurate quantitative analysis, we have performed Auger-peak simulations using well accepted procedures for the electron transport to the surface, incorporating continuous and plasmon energy losses and angular scattering [27]. The Auger source-spectrum inside the solid was derived from the DOS in Fig. 3, using a similar procedure as was previously applied by Houston et al. to electron-induced Auger spectra from graphite [26] (including the effects of static and dynamic initial-state screening). It is emphasized that only little information can be extracted from *electron-induced* Auger spectra alone. Since the transition energy and the transport cross-sections are not sufficiently well known and dependent on details of the amorphous carbon structure, we have varied them to fit this spectrum. As holds true for all weakly ionizing particles (X-rays or fast electrons), the target electron temperature is virtually $T_e = 0$ K. Thus, the electron-induced spectrum may serve as a reference for the ion data.

Consequently, the *ion-induced* spectra were analyzed by fitting simulated spectra to the experimental ones. All parameters were kept fix for these spectra, except for the electron temperature T_e. The resulting fit curves are shown as dashed and solid lines in Fig. 1. As can be seen, there is good agreement between the experimental and theoretical line shapes and the corresponding electron temperatures are shown in Fig. 6.

3. Thermal-spike model

If we restrict ourselves to times $\gg 1$ fs [22,23], we may apply thermodynamic concepts also to the theoretical treatment of electronic excitations close to the ion track. Quantitatively, when neglecting the inelastic interaction with the lattice (electron–phonon coupling and relaxation of the potential electron energy) the heat-diffusion equation for the electron temperature $T_e(\boldsymbol{r}, t)$ may be written as

$$C_e(T_e)\frac{\partial T_e}{\partial t} = \nabla(K_e(T_e) \cdot \nabla T_e) + A_e(\boldsymbol{r}, t), \tag{2}$$

where K_e is the electronic thermal conductivity, C_e the electronic heat capacity and $A_e(\boldsymbol{r}, t)$ the energy source-function. This equation describes the initial energy deposition in the electronic subsystem and the resulting heat diffusion before coupling with the atomic motion. Translational invariance of the track inside the bulk may be assumed because the projectile speed exceeds the speed of heat waves (Fermi velocity or somewhat higher at elevated temperatures) [28] by a factor of 10. Energy dissipation through ballistic heat waves may at least partially be included in A_e. The first quantitative model of this kind was worked out by Toulemonde and coworkers [9]. It is based on experimental data and free-electron estimates to obtain C_e and K_e as well as on an estimate for A_e that is correct only for large distances from the track. This model also includes the electron–phonon coupling which, however, is not important for times below 10 fs. In this work, we have improved the treatment by considering the actual DOS of amorphous carbon and its local fluctuations in the computation of C_e and K_e. K_e also incorporates a temperature dependent electron-transport cross-section. Furthermore, we have used a more advanced energy-deposition function A_e.

Before the results of Eq. (2) are shown, details of the basic ingredients are presented, namely the

parameters C_e, K_e and $A_e(\boldsymbol{r},t)$. An easy and straightforward computation is possible for the thermal capacity C_e, once the DOS is known. C_e is given by

$$C_e(T_e) = \int_0^\infty d\varepsilon\ (\varepsilon - E_{Fermi}) \frac{df}{dT}(\varepsilon, \mu, T_e) \times D(\varepsilon, T_{lattice}). \quad (3)$$

At low temperatures μ may be replaced by E_{Fermi} and for metals a peaking approximation is often used to place $D(E_{Fermi}, T_{lattice})$, the DOS at the Fermi level, in front of the integral. For high temperatures and for amorphous carbon, however, both approximations are not valid and thus, we have solved Eq. (3) directly with the DOS shown in Fig. 3 [24,25]. The results for C_e are shown as a solid line in Fig. 4 in comparison with free-electron-gas (FEG) estimates for a density of 3.9×10^{29} electrons/m^3 (dashed curve). Our C_e values lie below the FEG results because of the low electron density of a-C at the Fermi level. The experimental data [29,30] exceed C_e significantly, since they include the dominant heat capacity of the atomic subsystem.

The electronic thermal conductivity K_e and, for comparison purposes, the electrical conductivity $\sigma^{electric}$ are calculated in the relaxation-time approximation [31–33] from

$$K_e(T_e) = [F_3(T_e) - F_2^2(T_e)/F_1(T_e)]/T_e \quad (4)$$

assuming local thermodynamical equilibrium (zero net-particle flux) and from

$$\sigma^{electric}(T_e) = e_0^2 F_1(T_e) \quad (5)$$

with the generalized transport coefficients F_n of the type

$$F_n(T_e) = \frac{1}{3} \int v(\varepsilon) \varepsilon^{n-1} \frac{D^*(\varepsilon, T_{lattice})}{N_{atom}\sigma^{eff}(\varepsilon, T_e)} \times \frac{df}{d\mu}(\varepsilon, \mu, T_e)\, d\varepsilon, \quad (6)$$

where v is the electron velocity, N_{atom} the atomic density and σ^{eff} the effective transport cross-section per atom. The effective DOS D^* accounts for

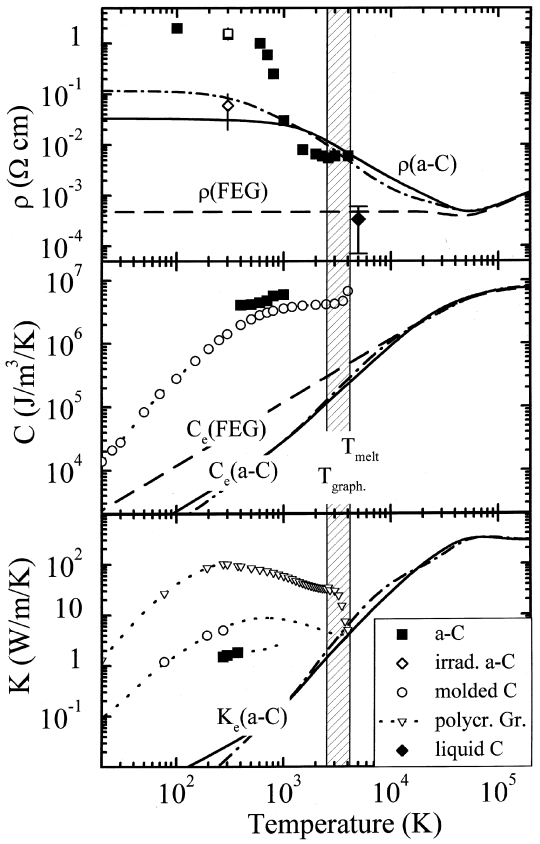

Fig. 4. Experimental specific resistivities ρ, heat capacities C and thermal conductivities K for different non-crystalline modifications of carbon (amorphous, irradiated, molded and liquid carbon as well as polycrystalline graphite) in comparison with theoretical results for the electronic fractions ρ, C_e and K_e in amorphous carbon (a-C) and for a FEG of the same electron density. The hatched area indicates the region where soft carbon types are graphitized (T_{graph}) up to the melting point (T_{melt}).

local fluctuations of the DOS that are treated with a simplified statistical ansatz. These fluctuations lead to a suppression of the electronic motion, the so-called Anderson localization [31–33]. The electrical conductivity is reduced by a factor of 11 at $T_e = 1000$ K and K_e is reduced by a factor of 8. Already at an electron temperature of 2×10^4 K, there is only a 10% influence on K_e and thus, the difference between D^* and D is of minor importance for the final results of the present work. The effective cross-section σ^{eff} in the above equation is obtained from the sum of the electron–electron

collision cross-section σ_{e-e} [34,37] (times the number of valence-band electrons per atom) accounting for the DOS of Fig. 3 and the elastic-scattering transport-contribution σ_{e-n}. The latter contribution is probably the most uncertain ingredient of the whole treatment and thus, it needs some additional explanations.

The electron–atom transport cross-section σ_{e-n} may be calculated from the partial-wave expansion of the scattering amplitude for a spherically averaged solid-state potential if interference effects with neighboring atoms are neglected. We have used two different methods to determine such a potential that have, in a similar way, successfully been applied to the analysis of extended X-ray absorption fine-structure (EXAFS) and low-energy electron diffraction (LEED) measurements [35,36]. In the first method, we have performed the self-consistent Hartree–Fock–Slater calculations with atomic boundary conditions, but with each wavefunction renormalized within the Wigner–Seitz radius. These renormalized wavefunctions are expected to be somewhat more accurate than the original Wigner–Seitz wavefunctions [37], but the node structure of valence-band electrons (2s in our case) is too strongly pronounced. In the second method, we have performed one extra iteration without renormalization and computed the spherical average of the summed electrostatic potentials as well as of the Kohn–Sham exchange potential for the summed electron density of about 100 atoms. This overlapped-atom potential (improved over the method by Mattheiss [38]) is expected to wash out node structures too strongly. Both methods, however, yield a net electron density consistent with amorphous carbon and in both cases we have replaced the potential outside the Wigner–Seitz radius by a constant that matches the value at the inner boundary of the sphere.

In order to describe finite temperatures, we have approximated the solid-state potential by using atomic excited state configurations in both methods. An example for such a configuration is $1s^2 2s^{1.1} 2p^{1.4} 3s^{0.2} 3p^{0.5} 3d^{0.8}$ that results from a fit to the Fermi–Dirac distribution at $T_e = 80,000$ K. For low temperatures the results of both methods deviate by a factor of two. For high electron temperatures, however, the two results for σ_{e-n} deviate by more than an order of magnitude. Thus, we have simply averaged both predictions, yielding the fitted T_e dependence of the transport cross-section σ_{e-n},

$$\sigma_{e-n}(T_e) = 10.3 \times 10^{-16} + 9.9 \times 10^{-16} \times \frac{1.33 \times 10^{18}}{1.33 \times 10^{18} + T_e^4}\ \mathrm{cm}^2. \quad (7)$$

This cross-section drops by a factor of two when the electron temperature exceeds 35,000 K. From test calculations with different cross-sections and different DOS, we expect to introduce uncertainties of $\pm 40\%$ for final electron temperatures around 2×10^4 K and $\pm 60\%$ for electron temperatures exceeding 5×10^4 K, mainly due to our approximate determination of the solid-state potential.

Fig. 4 displays the results for the electrical and thermal conductivity, calculated as described above. The solid lines incorporate the DOS by Galli et al. [24,25] (see Fig. 3) that is also used in our final calculations and the dashed–dotted curves rely on the DOS by Wang et al. [39]. Our theoretical electrical resistivity overestimates the experimental data by a factor of about two at temperatures of 1000–3000 K. At higher temperatures amorphous carbon undergoes a phase transformation. At temperatures below 1000 K the resistivity is sensitive to small variations of the DOS in the range $E_{Fermi} \pm 0.3$ eV and here we find strong deviations between experiment and theory. Judging from the deviation of both predictions of the DOS [24,25,39], a failure of the absolute magnitude of the DOS close to the Fermi level is easily conceivable. It is noted that the open square and the open diamond in Fig. 4 have been measured for our samples before and after extended irradiation with different beams. Thus, both DOS predictions seem to represent irradiated amorphous carbon structures. Liquid carbon has roughly the same DOS as a FEG and our prediction for this case is consistent with the averaged experimental data [24,25]. It is emphasized that the influence of the details of the DOS is not important for electron temperatures above 20,000 K.

Calculations for K_e have also been performed with both DOS. Below the melting point, there is a

strong influence of the atomic heat transport. This explains the deviations of our results from the experimental data for the total heat conductivity K [29,30]. Thus, our theoretical estimates are consistent with the experimental data for C_e, K_e as well as ρ, but uncertainties of a factor of two cannot be excluded.

The different contributions to the energy source-function $A_e(\boldsymbol{r}, t)$ are shown in Fig. 5 as a function of the distance to the track center. Calculations of ionization probabilities have been performed within perturbation theory, in the Magnus approximation and using the classical-trajectory Monte Carlo method [21,40]. From these calculations we have extracted the fractional kinetic energies of the ejected electrons and the contributions of the potential energy deposited in the K-shell and in the valence-band as well as the corresponding impact-parameter dependencies and the initial electron-energy spectra. Using a straight-line continuous-slowing-down model with corrections for the angular straggling, we have estimated the radial volume energy density from the energy loss of δ-electrons (deposited within about 0.1 fs) by considering the impact-parameter dependencies. These impact-parameter dependencies were also used together with the range of Auger electrons to estimate the potential-energy contributions in Fig. 5. This potential electronic energy is stored in vacancies produced by the incident ions. Such vacancies in the K-shell lead to the spectrum of ejected Auger electrons in Fig. 1, but most Auger electrons deposit their energy inside the solid. Vacancies in the valence band are also filled by low energetic Auger type transitions and the corresponding energy is dissipated very close to the ion track. For the computation of this part of the energy source-function, average decay times of 1 and 10 fs are assigned to Auger electrons from the valence band and from the K-shell x(averaged over both types of KVV transitions), respectively.

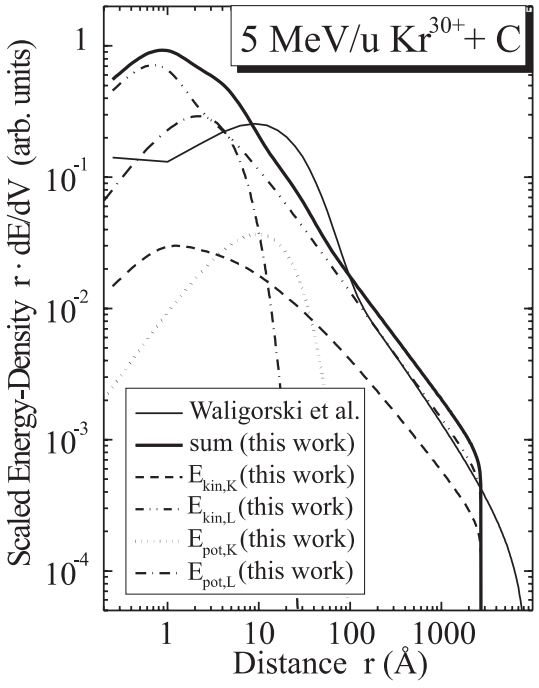

Fig. 5. Electronic energy deposition as function of the distance to the center of the ion track. The contributions from K and L electrons are shown separately as well as the kinetic-energy fractions due to fast δ-electrons (E_{kin}) and the potential electronic energy (E_{pot}) released by different types of Auger transitions (see text). The sum of all contributions is plotted as a thick solid curve in comparison with the semi-empirical distribution by Waligorski et al. (thin solid curve).

As can be seen from the plot, the contribution due to fast δ-electrons ejected from the K-shell is small. For radial distances around 10 Å, however, the other three contributions (δ-electrons from the valence band and Auger decay from both bands) are of similar importance. The influence of Auger transitions is even somewhat enlarged due to the finite decay times and the corresponding delayed release of excitation energy.

The total deposited energy is shown as a thick solid curve in Fig. 5. This result may be compared to a semi-empirical solution (thin solid curve) that has become a standard in radiation dosimetry [41]. It is noted that the simple formula [41] is more appropriate for distances near the boundary of the ultra track (about 4000 Å), since angular scattering of δ-electrons has been accounted for. Where the present model, however, yields finite volume energy densities do the other results diverge at $r = 0$, since the impact parameter dependence has been neglected there. Nevertheless, the energy deposited in the first 10 Å, responsible for the transient

temperature rise in the track, is significantly higher in our model than the one given by the semi-empirical distribution.

4. Results and discussion

Finally, we present and discuss the electron temperatures T_e extracted from the experimental Auger electron spectra in comparison with the results of the present thermal-spike model and the one of Toulemonde et al. The squared symbols in Fig. 6 represent results that have been determined from the shape of the K^2VV emission and the circles correspond to the K^1VV Auger-decay. The open symbols show our new results and the closed symbols have been published recently [17,18]. The error bars include the uncertainties of the fitting procedure as well as an estimate of systematic errors of the analysis.

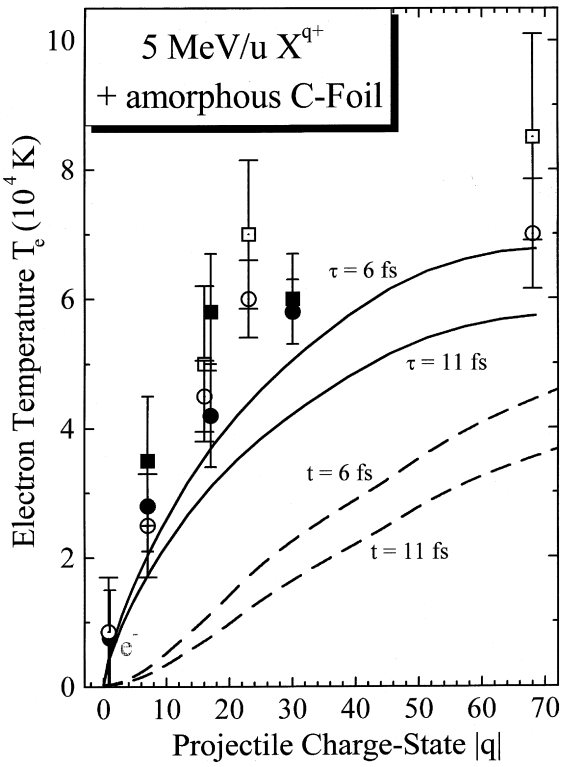

Fig. 6. Electron temperatures as extracted from the experimental K^1VV (circles) and K^2VV (squares) Auger-data in Fig. 1 in comparison with results of two thermal-spike models for the corresponding decay times: solid curves (this work) and dashed curves (using the program of Toulemonde et al. with free electron estimates).

The experimental electron temperatures for both transitions increase roughly with the square root of the projectile charge. A similar q dependence of T_e can be estimated from a simple thermodynamical description. If we neglect any heat transport in the solid, the integrated electronic heat capacity C_e (the internal energy) is proportional to the stopping power S_e of the ions. For amorphous carbon we find $\int dT_e C_e \propto T_e^{2.3}$ and $\propto T_e^2$ for a FEG. Furthermore, $S_e \propto q^{1.7}$ for the ions in this investigation ($S_e \propto q^2$ for very light ions). From the above dependencies, it directly follows that $T_e \propto q^{1.7/2.3} \approx q^{0.7}$ in the present case, which is close to our experimental finding.

Note that the more accurate values of $T_e(K^1VV)$ determined for Ar^{16+} projectiles and Kr^{17+} ions (the only non-equilibrium charge state used in this investigation) are nearly the same, although the projectile nuclear charges differ considerably. Thus, T_e seems to depend only on the incident charge state. This is also expected, since the projectile charge state is conserved over a penetration depth of about 25 Å for these fast heavy ions, whereas the high-energy slope of the Auger peak is sensitive only to the first 10 Å below the surface.

Thermal-spike calculations were performed within the above described model (solid curves) as well as with the FEG program by Toulemonde and coworkers [9] (dashed curves). For both models results were calculated for $r = 0$, the center of the track. The FEG results are plotted for the time evolution at $t = 6$ and 11 fs after the ion passage, corresponding to the K^2VV and the K^1VV Auger-decay time, respectively. The results of our code have been averaged over an exponential decay, with time constants of $\tau = 6$ and 11 fs. This averaging procedure increases the effective electron temperature by about 20%. We verified the consistency of both programs by using the assumptions of Toulemonde et al. as a test case also in our code. The calculated radial temperature distributions reach half widths of 10 Å and above. Thus, many electrons share the

deposited energy, consistent with the initial assumption of a local thermodynamical equilibrium in the electron system.

The present model results underestimate the experimental data by about 30%. The FEG model underestimates the temperatures by a factor of two for heavy ions and by more than an order of magnitude for light ions. The reason for this significant disagreement of this model is the neglect of a realistic DOS for the parameters K_e and C_e as well as an underestimated energy deposition close to the center of the track.

The remaining discrepancies between the present model results and the data might be related to uncertainties of K_e or of the thermodynamical description. It is, however, also conceivable that the influence of the surface or of the extraordinary high excitation of the Auger emitter are influencing the measured temperature.

Finally, one may compare experimental and theoretical cooling times. Assuming an exponential temperature decay, we extract an experimental time constant of $\tau_T = 34 \pm 14$ fs from the K^2VV and the K^1VV Auger transitions. This is consistent with our theoretical result (29 to 34 fs dependent on the projectile charge). The FEG thermal-spike model by Toulemonde et al. yields 12 to 26 fs under the same conditions. These values seem to be somewhat too low in comparison with the experimental data. It is noted that the temperature dependence of the transport cross-section (Eq. (7)) increases the cooling time in our model significantly.

5. Conclusions

In this work we investigated the peak position, the intensity as well as the shape of target KVV Auger electron spectra from amorphous carbon. Measurements were performed for electrons, N^{7+} and Ar^{16+} ions at 5 MeV/u and previous Ni^{23+} and U^{68+} spectra were reanalyzed. The analyses allows one to extract the following scenario of electronic energy deposition and dissipation close to the ion track.

- Initially, at $t = 0$ the target atoms are highly ionized and for projectile charge states $q > 25$ there is complete ionization of all electronic bands of carbon in the center of the track (impact parameter zero).
- Charge neutralization occurs rapidly in this material and an upper boundary of $\tau_{CN} < 0.3$ fs is consistent with the present results as well as with previous convoy electron measurements and theoretical estimates.
- The charge-neutralization processes lead to a population of excited conduction-band states that may be described by a Fermi–Dirac distribution. Electron temperatures of up to 80,000 K were determined for two different Auger transitions (K^1VV and K^2VV) corresponding to snapshots of the recombination sequence around 6 and 11 fs after the passage of the ion.
- Afterwards, the electron system cools down with a time constant of $\tau_T \cong 34$ fs, as we have determined from the ratio of temperatures at two different times.

The comparison between the experimental and theoretical results for the electron temperature looks promising. It is emphasized, however, that the theoretical treatment so far neglects surface effects and the determination of the thermodynamical properties of amorphous carbon introduces some uncertainties. Our theoretical results underestimate the experimental data for all projectiles by about 30%. At present it is not clear whether this deviation is typical for amorphous carbon only or whether we are facing an intrinsic error of the thermal-spike model. Thus, further studies for other materials such as semiconductors and FEG like metals are needed to test the model assumptions.

Acknowledgements

We are indebted to W. Bohne and J. Röhrich for the elastic-recoil detection analysis of the target stoichiometry. Furthermore, we thank C. Dufour and M. Toulemonde for leaving us a copy of their program code and S. Klaumünzer as well as J. Schou and M. Rösler for their helpful discussions. We also acknowledge the support of one of the authors (P.L.G.) by the Alexander-von-Humboldt foundation.

References

[1] R.L. Fleischer, P.B. Price, R.M. Walker, Nuclear Tracks in Solids, University of California Press, Berkely California, 1975.
[2] R. Spohr, Ion tracks and microtechnology, F. Vieweg und Sohn Verlagsgesellschaft, Braunschweig, 1990.
[3] J.P. Biersack, E. Santner, Nucl. Instr. and Meth. 132 (1976) 229.
[4] J.P. Biersack, E. Santner, Nucl. Instr. and Meth. 198 (1982) 29.
[5] C. Trautmann, M. Toulemonde, K. Schwartz, J.M. Costantini, A. Müller, Nucl. Instr. and Meth. B 164–165 (2000) 365.
[6] S. Klaumünzer, M.-d. Hou, G. Schumacher, Phys. Rev. Lett. 57 (1986) 850.
[7] P. Stampfli, K.H. Bennemann, Phys. Rev. B 49 (1994) 7299.
[8] P. Stampfli, Nucl. Instr. and Meth. B 107 (1996) 138.
[9] Z.G. Wang, C. Dufour, E. Paumier, M. Toulemonde, J. Phys. 6 (1994) 6733.
[10] A.E. Volkov, V.A. Borodin, Nucl. Instr. and Meth. B 107 (1996) 172.
[11] G. Xiao, G. Schiwietz, P.L. Grande, A. Schmoldt, N. Stolterfoht, M. Grether, R. Köhrbrück, A. Spieler, U. Stettner, Phys. Rev. Lett. 79 (1997) 1821.
[12] G. Schiwietz, G. Xiao, P.L. Grande, N. Stolterfoht, A. Schmoldt, M. Grether, R. Köhrbrück, A. Spieler, U. Stettner, Scanning Microscopy International, review paper, accepted for publication.
[13] G. Schiwietz, P.L. Grande, B. Skogvall, J.P. Biersack, R. Köhrbrück, K. Sommer, A. Schmoldt, P. Goppelt, I. Kádár, S. Ricz, U. Stettner, Phys. Rev. Lett. 69 (1992) 628.
[14] G. Schiwietz, G. Xiao, Nucl. Instr. and Meth. B 107 (1996) 113.
[15] G. Schiwietz, G. Xiao, P.L. Grande, A. Schmoldt, M. Grether, R. Köhrbrück, A. Spieler, U. Stettner, Scanning Microscopy International, in print.
[16] K. Wien, Ch. Koch, Nguyen van Tan, Nucl. Instr. and Meth. B 100 (1995) 322.
[17] G. Schiwietz, G. Xiao, P.L. Grande, E. Luderer, R. Pazirandeh, U. Stettner, Nucl. Instr. and Meth. B 146 (1998) 131.
[18] G. Schiwietz, G. Xiao, P.L. Grande, E. Luderer, R. Pazirandeh, U. Stettner, Eurohys. Lett. 47 (1999) 384.
[19] G. Schiwietz, D. Schneider, J.P. Biersack, N. Stolterfoht, D. Fink, A. Mattis, B. Skogvall, H. Altevogt, V. Montemayor, U. Stettner, Phys. Rev. Lett. 61 (1988) 2677.
[20] D. Schneider, G. Schiwietz, D. De Witt, Phys. Rev. A 47 (1992) 3945.
[21] G. Schiwietz, P.L. Grande, Radiat. Eff. Def. in Solids 130/131 (1994) 137, and references therein.
[22] E. Knoesel, A. Hotzel, T. Hertel, M. Wolf, G. Ertl, Surf. Sci. 368 (1996) 76.
[23] M. Aeschlimann, M. Bauer, S. Pawlik, Chem. Phys. 205 (1996) 127.
[24] G. Galli, R.M. Martin, R. Car, M. Parrinello, Phys. Rev. B 42 (1990) 7470.
[25] J. Schäfer, J. Ristein, R. Graupner, L. Ley, U. Stephan, Th. Frauenheim, V.S. Veerasamy, G.A.J. Amaratunga, M. Weiler, H. Erhardt, Phys. Rev. B 53 (1996) 7762.
[26] J.E. Houston, J.W. Rogers, R.R. Rye, F.L. Hutson, D.E. Ramaker, Phys. Rev. B 34 (1986) 1215.
[27] S. Tougaard, P. Sigmund, Phys. Rev. B 25 (1982) 4452.
[28] S.D. Brorson, J.G. Fujimoto, E.P. Ippen, Phys. Rev. Lett. 59 (1987) 1962.
[29] D.R. Lide (Ed.), CRC Handbook of Physics and Chemistry, CRC Press, Boston, 1992.
[30] Gmelins Handbuch der anorganischen Chemie, Vol. 14, Verlag Chemie, Weinheim, 1967.
[31] J. Callaway, Quantum Theory of the Solid State, Part B, Academic Press, New York, 1974.
[32] A. Sommerfeld, Thermodynamik und Statistik, Vol. 5, Verlag Harri Deutsch, Frankfurt, 1977.
[33] W. Jones, N.H. March, Theoretical Solid-State Physics, Vol. 2, Wiley-Interscience, London, 1973.
[34] Yu.V. Martynenko, Yu.N. Yavlinskii, Sov. Phys. Dokl. 28 (1983) 391.
[35] J.B. Pendry, Low-Energy Electron Diffraction, Academic Press, London, 1974.
[36] J.M. de Leon, J.J. Rehr, S.I. Zabinky, R.C. Albers, Phys. Rev. B 44 (1991) 4146.
[37] C. Kittel, Introduction in Solid-State Physics, Vol. 7, Oldenburg Verlag, München, 1988.
[38] L. Mattheiss, Phys. Rev. 133 (1964) A1399.
[39] C.Z. Wang, K.M. Ho, C.T. Chan, Phys. Rev. Lett. 70 (1993) 611.
[40] P.L. Grande, G. Schiwietz, J. Phys. B 28 (1995) 425.
[41] M.P.R. Waligorski, R.N. Hamm, R. Katz, Nucl. Tracks Radiat. Meas. 11 (1986) 309.